Controllable synthesis and morphology-dependent microwave absorption properties of iron nanocrystals

**Qiangchun Liu · Zhenfa Zi · Dajun Wu ·
Yuping Sun · Jianming Dai**

Abstract Iron nanospheres, nanoflakes and nanofibers were synthesized via a simple pyrolysis method. When the pyrolysis temperature increased from 523 to 623 K and the flow rate of Ar carrier gas maintained at 100 sccm, the as-prepared iron nanocrystals showed a morphology evolution from isotropic nanospheres to isotropic nanofibers. The phase structures and morphologies of the composite were characterized by X-ray diffraction and scanning electron microscopy. The complex permittivity ($\varepsilon' - j\varepsilon''$) and permeability ($\mu' - j\mu''$) of these composites were measured using the transmission/refection coaxial line method in the frequency range of 1–18 GHz by a vector network analyzer. The iron nanofibers exhibited superior microwave absorbing properties compared to iron nanoparticles and nanoflakes. The optimal reflection loss (RL) reached −17.8 dB at 9.9 GHz with a layer thickness of 2.0 mm. The RL below −10 dB can be obtained in the frequency range of 7.3–11.7 GHz. Considering the low cost and high efficiency; the iron nanofibers are favorable for application as microwave absorber.

Q. Liu · Z. Zi · D. Wu · Y. Sun · J. Dai (✉)
Key Laboratory of Materials Physics, Institute of Solid State Physics, and Hefei High Magnetic Field Laboratory, Chinese Academy of Sciences, Hefei 230031, People's Republic of China
e-mail: jmdai@issp.ac.cn

Q. Liu · Z. Zi
School of Physics and Electronics Information, Huaibei Normal University, Huaibei 235000, Anhui, People's Republic of China

Introduction

In recent years, with the use of GHz electromagnetic waves in wireless communications, satellite communications, radar systems and military applications, several problems such as an electromagnetic interference and information leakage have emerged [1]. Thus, the development of the microwave absorbing materials (MAMs) is now strongly demanded [2–6]. Generally, the electromagnetic absorbing performance of any MAM is linked to its intrinsic electromagnetic properties (i.e., conductivity, complex permittivity and permeability) as well as to extrinsic properties such as the thickness and working frequencies [7]. Majority of the MAMs are composed of magnetic powders such as ferrite, nickel, alloys and other dielectric loss materials such as carbon materials, conducting polymers [8–12]. Among the candidates for electromagnetic wave absorbers, metallic soft magnets are particularly interesting [13–15] because they have larger saturation magnetization values than ferrites [16]. Iron nanowires are regarded as one of the most promising materials for the electromagnetic wave absorber in the GHz range due to their high permeability and shape anisotropy [17]. Therefore, it is possible to make thin absorbers in gigahertz range. Several methods, including thermal and sonochemical decomposition of organo-metallic precursors [18], high-temperature reduction of metal salts [19] and chemical vapor condensation of organometallic precursors [20], have been applied to fabricate iron nanowires. However, they showed unavoidable disadvantages of complicated multisteps, toxic iron-containing metal–organic complexes, harsh synthesis conditions (e.g., high temperature) and high-cost.

In this paper, the main objective is to develop a simple method to control size and morphology by tuned fabrication of iron nanostructures. For such a purpose, iron nanospheres, nanoflakes and nanofibers were synthesized via a simple pyrolysis method.

Experimental

Synthesis of iron nanocrystals

Fe(CO)$_5$ (99.7%) was purchased from Jiangsu Tianyi Ultra-fine metal powder Co., Ltd. The aluminum substrate (8 cm in length and 4 cm in width) was sonicated in acetone for 10 min, followed by repeated rinsing with distilled water. In a typical procedure, a long aluminum plate was placed at the center to act as the deposition substrate. Ten milliliter Fe(CO)$_5$ was placed at a ceramic boat which was inserted at the entrance of the horizontal quartz tube furnace (8 cm in inner diameter and 100 cm in length, equipped with temperature and gas-flow controller). The horizontal distance between the ceramic boat and the aluminum substrate was maintained at 30 cm. The pyrolysis of Fe(CO)$_5$ was carried out at a selected temperature (523 or 623 K) for 1 h in a flowing atmosphere of Ar which act as both protecting medium and carrying gas. The furnace temperature was allowed to cool down to room temperature naturally before the product was taken out. Alternatively, as the flow rate of Ar carrier gas (50–400 sccm, sccm denotes standard cubic centimeters per minute) and the temperature (523 or 623 K) changed, the morphology of the products also changed.

Characterization

The phase identification was performed by X-ray diffraction (XRD) on a Bruker Advance D8 X-ray diffractometer with CuKα radiation ($\lambda = 1.5418$ Å) in the range from $2\theta = 15°$ to $85°$ with a scanning rate of $5°/min$. The morphologies and surface characteristics were observed by JEOL-6610LV scanning electronic microscopy (SEM). The as-prepared iron nanocrystals were mixed uniformly with molten paraffin wax with a ratio of 50 wt% and molded into toroidal-shaped specimens for microwave tests. The coaxial cylindrical specimen had an outer diameter of 7.00 mm and inner diameter of 3.04 mm. The scattering parameters (S11, S21, S22, S12) of the paraffin compacts were measured by a vector network analyzer (VNA, AV3629D) in the range of 1–18 GHz after a full two-port calibration (SHORT-OPEN-LOAD-THRU).

Results and discussion

The phase purity of the as-synthesized iron nanofibers was investigated using XRD. As shown in Fig. 1, the 2θ values at 44.35°, 64.53° and 81.66° could be indexed to the (110), (200) and (211) planes of a body-centered cubic α-Fe with the lattice constant a = 2.884 Å (PDF-2 entry: 85-1410, space group: *Im3m*). No impurities such as α-Fe$_2$O$_3$, γ-Fe$_2$O$_3$ or Fe$_3$O$_4$ were observed in XRD pattern.
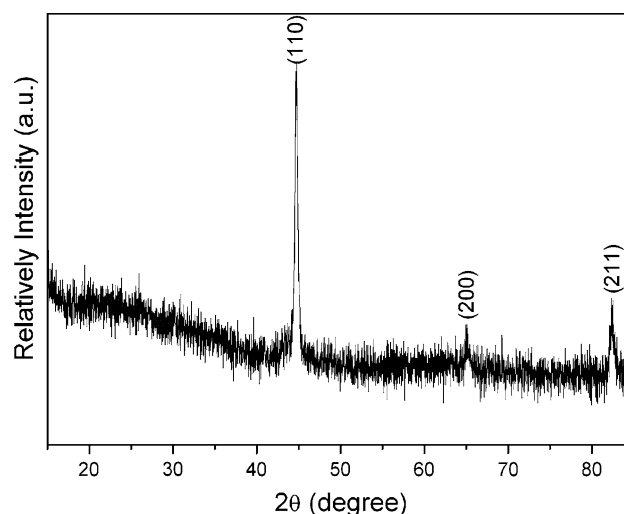

Fig. 1 XRD pattern of the as-synthesized iron nanofibers

The morphologies of the samples synthesized under different reaction conditions are shown in Fig. 2. A typical SEM image of the product pyrolysis at 523 K for 2 h at a carrier gas rate of 50 sccm is presented in Fig. 1a, which shows that the particles are sphere-like and each sphere has a diameter in the range of 80–120 nm. This can be explained by considering that at a relatively high temperature [higher than the decomposition temperature of Fe(CO)$_5$], the iron nuclei will form before the growth process starts. After a period of time, the nuclei aggregate together and form the sphere-like iron nanoparticles. When the carrier gas rates increases to 100 sccm, a larger mount of iron nuclei were produced from the decomposition of Fe(CO)$_5$. Compared with iron nanospheres obtained at 50 sccm, these nanospheres (Fig. 2b) obtained at 100 sccm have a larger average diameter and some nanospheres aggregate together. As the carrier gas rate increased to 200 sccm, all the iron spheres aggregate together (Fig. 2c). From this image, it can be observed that the surface of the iron spheres is not smooth. It is built-up of many small nanoparticles, which makes the spheres look very rugged. These small nanoparticles constitute many active positions on the surface and make the spheres with a larger surface area than that of smooth spheres. It makes the site of each small nanoparticles act as nucleation centers for a daughter generation. When the carrier gas rates increases to 300 sccm, the sphere-like iron particles become larger and produce a daughter generation nanospheres (Fig. 2d). The inset image in Fig. 2d is a higher magnification image. From the image, we can clearly observe many daughterly nanospheres with the diameter of about 60–80 nm. On the basis of the results mentioned above, it can be clearly seen that the carrier gas rate, which was related to the carrying quantity of Fe(CO)$_5$ into the quartz tube, has great influence on the morphology of the final product in the present route.
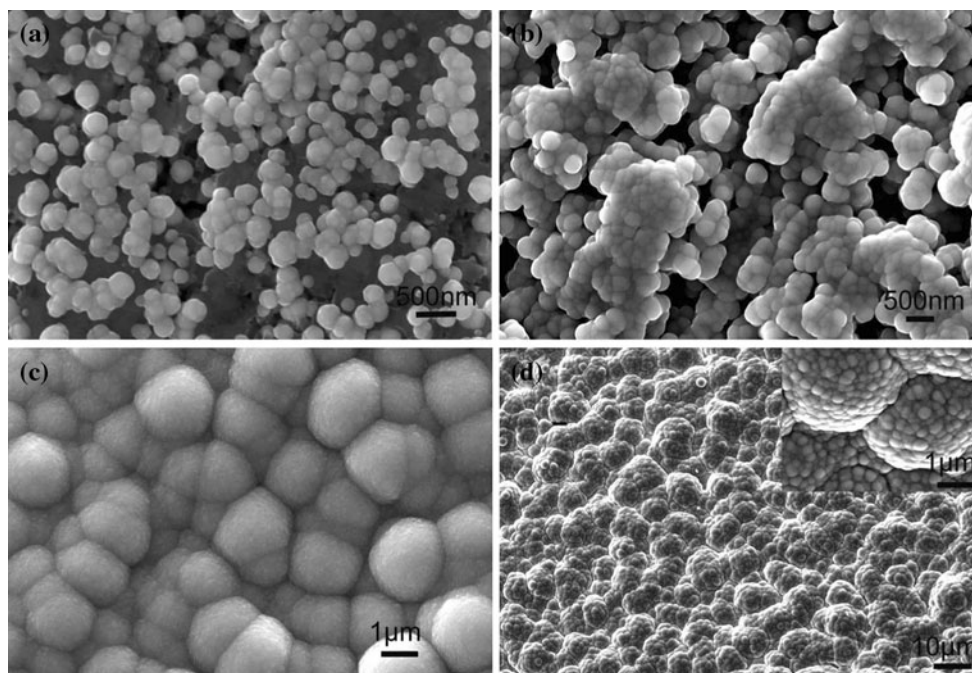
Fig. 2 SEM images of iron nanocomposites pyrolysis at 523 K for 2 h in different Ar carrier gas rates **a** 50 sccm, **b** 100 sccm, **c** 200 sccm, **d** 300 sccm, *inset* the corresponding image in high magnification
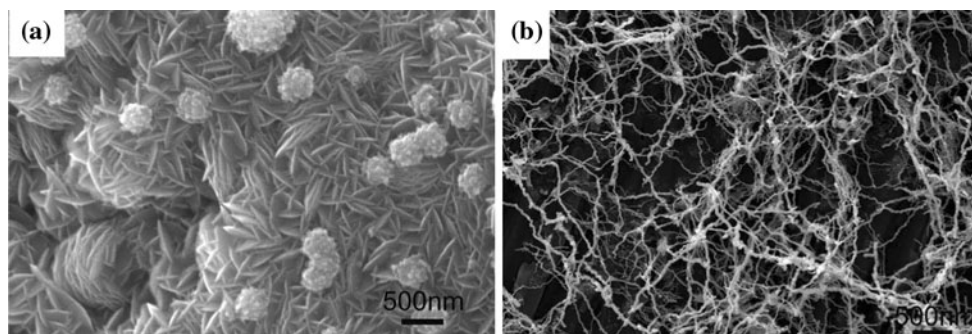

Fig. 3 SEM images of iron nanocomposites pyrolysis at 623 K in different carry gas rates **a** 50 sccm, **b** 100 sccm

When the furnace temperature increased to above 623 K and the flow rate of Ar carrier gas was maintained at 50 or 100 sccm, the iron nanoflakes or nanofibers were obtained, respectively (Fig. 3). From Fig. 3a, it can be seen that the sample includes large amounts of flake-like structure with the thickness of about 30–50 nm. In contrast, increasing flow rate of Ar carrier gas (100 sccm), iron nanofibers are obtained. Figure 3b indicates that most of the iron nanofibers are about 30 nm in diameter and 30 μm in length, with an aspect ratio of 1,000. The plausible formation processes for the 1D fiber-like iron nanostructures are schematically illustrated as follows. When the furnace temperature increased to above 623 K, $Fe(CO)_5$ can decompose to iron nuclei in a short time. These iron nuclei aggregate to the aluminum substrate and form the iron nanoparticles. At this moment, the temperature of the iron nanoparticles rapidly increases to 623 K. Subsequently, the $Fe(CO)_5$ will decompose on the surface of iron nanoparticles and gradually attach to the iron nanoparticles instead of the aggregation. Therefore, 1D iron nanofibers are formed by the anisotropic growth.

Figure 4a and b show real part (ε') and imaginary part (ε'') of the relative complex permittivity of the composites containing 50 wt% iron dispersed in a paraffin matrix in the frequency range of 1–18 GHz. The ε' and ε'' represent the energy storage ability and loss ability, respectively. The ε' and ε'' of iron nanoflakes and nanospheres are almost constant with nearly no variation throughout the whole frequency range. For the iron nanoflakes, the ε' and ε'' values decrease from 40.1, 17.7 to 26.9, 8.3 in the measured frequency range, respectively. The notable increase of complex permittivity for iron nanofibers could be
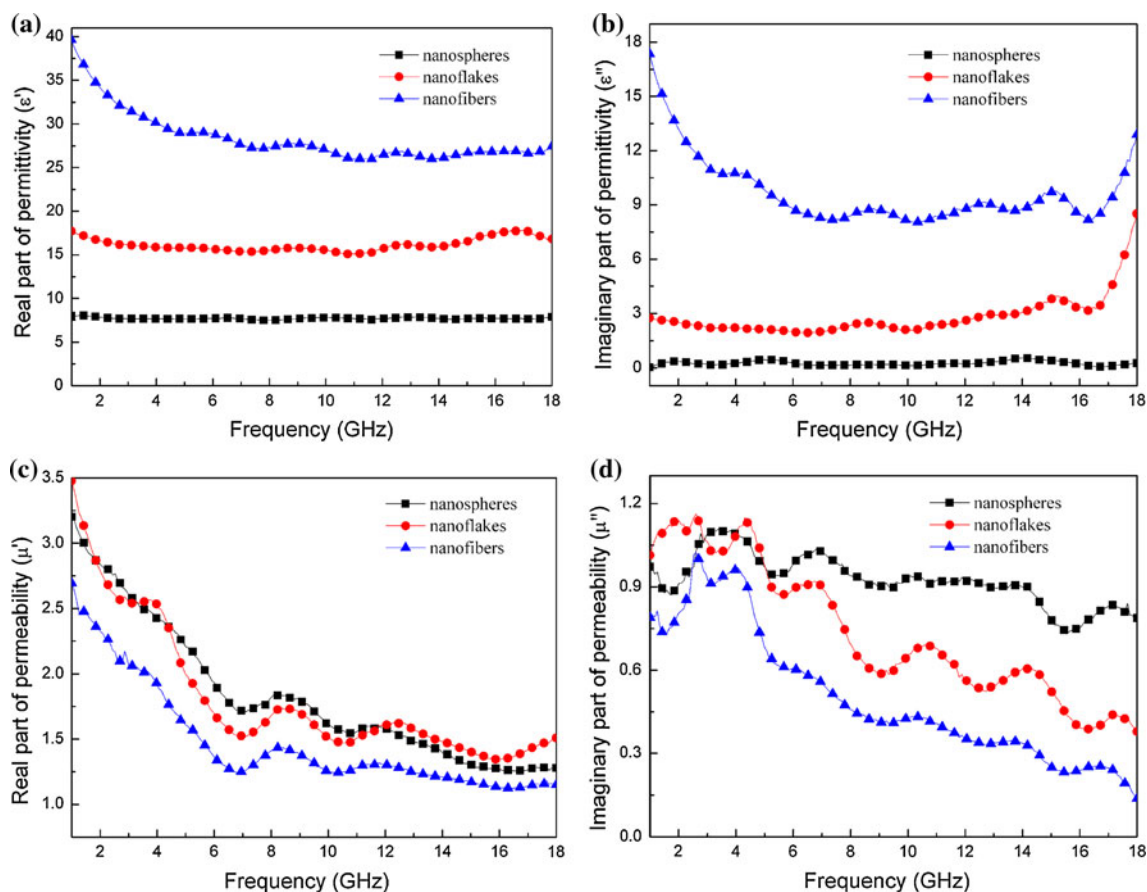
Fig. 4 The frequency dependence real part ε' (**a**), imaginary part ε'' (**b**) of complex permittivity and real part μ' (**c**), imaginary part μ'' (**d**) of complex permeability

attributed to the resistivity and space-charge polarization. On one hand, according to the free electron theory, $\varepsilon'' = 1/\rho\omega\varepsilon_0$, where ω, ε_0 and ρ are the angular frequency, the dielectric constant of free space, and the resistivity, respectively, from which it can be speculated that iron nanoflakes and nanospheres have higher electric resistivity than iron nanofibers. On the other hand, the space-charge polarization in heterogeneous systems with high-aspect ratio nanofibers is enhanced when compared to that of nanoflakes or nanospheres. It can be seen that both ε' and ε'' of iron nanofibers are obviously enhanced, which plays a dominant role in determining the dielectric loss properties. Figure 4c and d show real part (μ') and imaginary part (μ'') of the relative complex permeability of iron nanocrystals. The μ' values of iron nanocrystals exhibit an abrupt decrease in the 1–7 GHz and retain an approximate constant over 10–18 GHz. The μ'' curve exhibits a peak in the 1–6 GHz range for all the iron nanocrystals, which attributes to natural resonance. In comparison with Fe bulk material ($f_r = 1.6$ GHz) [21], the magnetic natural resonance of iron nanocrystals shifted to higher frequency. As we know, the anisotropic magnetic particles may have a

higher resonance frequency above Snoek's limit in the gigahertz frequency range due to their low eddy current loss coming from the particle shape effects. The skin depth of ferromagnetic iron at microwave frequencies is about 1 mm which was much larger than the diameters of Fe nanowires, Fe nanospheres and Fe nanoflakes. Thus, the eddy current loss due to the skin effect was massively suppressed in all samples. Besides the main resonance peaks, there are some minor fluctuations on the spectra, which might attribute to inhomogeneous particles size.

The electromagnetic reflection loss of samples is simulated by the transmission line theory. The reflection loss (RL) curves at the given frequency and the matching absorber thickness are calculated as follows [22]:

$$Z_{in} = Z_0 \sqrt{\mu_r / \varepsilon_r} \tanh\{j(2\pi f d / c)\sqrt{\mu_r \varepsilon_r}\} \quad (1)$$

$$R_L(dB) = 20\log\left|\frac{Z_{in} - Z_0}{Z_{in} + Z_0}\right| \quad (2)$$

where μ_r and ε_r are the relative permeability and permittivity, respectively, f is the frequency of incident electromagnetic wave, d is the absorber thickness, c is the velocity
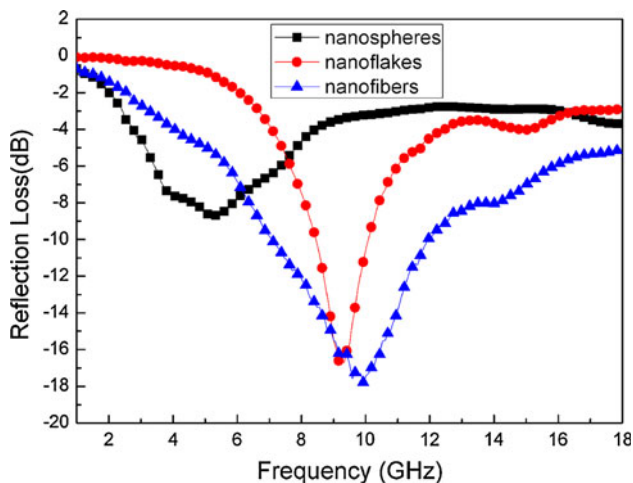
Fig. 5 Reflection loss with a thickness of 2.0 mm

of light, Z_0 is the impedance of free space (376.7 Ω), and Z_{in} is the input impedance of absorber.

For the purpose of comparing the microwave absorption properties of iron nanocrystals with different morphologies, the relations of matching frequency and reflection loss were researched. Figure 5 shows the simulation of reflection loss versus frequency employing the electromagnetic parameters at the thickness of 2 mm. It can be seen that an optimal RL reached −17.8 dB at 9.9 GHz for the iron nanofibers, while the absorption exceeding −10 dB (>90% power absorption) is obtained in the 7.3–11.7 GHz range. The iron nanospheres exhibit reflection loss about −8.5 dB at 5.2 GHz. Although the iron nanoflakes exhibit reflection loss −16.6 dB at 9.3 GHz, the absorption exceeding −10 dB is only obtained in the 8.5-10.4 GHz range. The results indicate that the morphologies of iron nanomaterials have an obvious effect on the reflection loss of composites. The optimal RL and bandwidth are increased with larger aspect ratio. As we know, there are mainly two possible contributions for microwave absorption, namely magnetic loss and dielectric loss. The enhancement of microwave properties of iron nanofibers attributes to the improvement of dielectric loss as discussed above.

Conclusions

In conclusion, iron nanocrystals with spherical, flaky and fiber-like shapes were successfully fabricated through a simple pyrolysis method, respectively. When the pyrolysis temperature increased from 523 to 623 K and the flow rate of Ar carrier gas maintained at 100 sccm, the as-prepared iron nanocrystals showed a morphology evolution from isotropic nanospheres to isotropic nanofibers. The complex permittivity of anisotropic iron nanofibers was higher than that of isotropic iron nanospheres, while the complex permeability showed a similar variation trend. The iron nanofibers exhibited superior microwave absorbing properties compared to iron nanoparticles and nanoflakes. The optimal reflection loss reached −17.8 dB at 9.9 GHz with a layer thickness of 2.0 mm. The reflection loss below −10 dB can be obtained in the frequency range of 7.3–11.7 GHz. The reflection loss calculations show that the prepared iron nanofibers are good electromagnetic wave absorbers in the microwave range. Thus, the iron nanofibers could be used as a kind of candidate absorber.

References

1. Sugimoto S, Maeda T, Book D, Kagotani T, Inomata K, Homma M, Ota H, Houjou Y, Sato R (2002) J Alloys Compd 330:331
2. Che RC, Peng LM, Duan XF, Chen Q, Liang XL (2004) Adv Mater 16:401–405
3. Yuan CL, Hong YS (2010) J Mater Sci 45:3470. doi:10.1007/s10853-010-4375-x
4. Cheng YL, Dai JM, Zhu XB, Wu DJ, Yang ZR, Sun YP (2009) Nanoscale Res Lett 4:1153
5. Yan LG, Wang JB, Han XH, Ren Y, Liu QF, Li FS (2010) Nanotechnology 21:095708
6. Liu QC, Dai JM, Zi ZF, Wu DJ, Sun YP (2011) Adv Mater Res 239–242:1725
7. Darwish MSA, Peuker U, Kunz U, Turek T (2011) J Mater Sci 46:2123. doi:10.1007/s10853-010-5048-5
8. Wang J, Xu HF, Song JW, Zhang HJ, Gao BL, Huang YD (2011) J Mater Sci 46:2955. doi:10.1007/s10853-010-5171-3
9. Zhao HT, Zhang B, Zhang JS, Zhang LF, Han XJ, Xu P, Zhou Y (2010) J Phys Chem C 114:21214
10. Liu XG, Ou ZQ, Geng DY, Han Z, Jiang JJ, Liu W, Zhang ZD (2010) Carbon 48:891
11. Zhou JH, He JP, Li GX, Wang T, Sun D, Ding XC, Zhao JQ, Wu SC (2010) J Phys Chem C 114:7611
12. Huo J, Wang L, Yu H (2009) J Mater Sci 44:3917. doi:10.1007/s10853-009-3561-1
13. Wang C, Han XJ, Zhang XL, Hu SR, Zhang T, Wang JY, Du YC, Wang XH, Xu P (2010) J Phys Chem C 114:14826
14. Liu QL, Zhang D, Fan TX (2008) Appl Phys Lett 93:013110
15. Yang RB, Liang WF, Lin WS, Lin HM, Tsay CY, Lin CK (2011) J Appl Phys 109:07B527
16. Snoek JL (1948) Physica 14:207
17. Liu JR, Itoh M, Terada M, Horikawa T, Machida K (2007) Appl Phys Lett 91:093101
18. Suslick KS, Fang M, Hyeon T (1996) J Am Chem Soc 118:11960
19. Fan X, Guan JG, Wang W, Tong GX (2009) J Phys D Appl Phys 42:075006
20. Park SJ, Kim S, Lee S, Khim ZG, Char K, Hyeon T (2000) J Am Chem Soc 122:8581
21. Ma J, Li JG, Ni X, Zhang XD, Huang JJ (2009) Appl Phys Lett 95:102505
22. Naito Y, Suetake K (1971) IEEE Trans Microwave Theory Tech 19:65